crystals

Article

Novel Quaternary Ammonium Aldimine Derivatives Featuring 3,4,5-Trimethoxy Phenyl Fragment: Synthesis, Crystal Structure and Evaluation of Antioxidant and Antibacterial Activity

Rusi Rusew [1,*], Mariya Georgieva [1], Vanya Kurteva [2] and Boris Shivachev [1]

[1] Institute of Mineralogy and Crystallography "Acad. Ivan Kostov", Bulgarian Academy of Sciences, Acad. G. Bonchev Street, bl. 107, 1113 Sofia, Bulgaria; mgeorgieva@imc.bas.bg (M.G.); blshivachev@gmail.com (B.S.)
[2] Institute of Organic Chemistry with Centre of Phytochemistry, Bulgarian Academy of Sciences, Acad. G. Bonchev Street, bl. 9, 1113 Sofia, Bulgaria
* Correspondence: r.rusev93@gmail.com

Abstract: This study demonstrates the synthesis of five novel quaternary ammonium aldimines through a two-step synthetic route involving a condensation reaction between 4-pyridincarboxyaldehyde and 3,4,5-trimethoxyaniline, followed by the quaternization of the pyridine N-atom with various aromatic α-bromo ketones. The newly obtained compounds underwent characterization for both purity and molecular structure, utilizing HR-MS, 1D, and 2D NMR spectroscopy in solution, as well as a comparison between single-crystal and powder X-ray analyses in a solid state. The thermal behavior of the studied compounds was evaluated using differential scanning calorimetry (DSC). The antioxidant properties of the compounds were assessed through DPPH (2,2-diphenyl-1-picrylhydrazyl) radical scavenging and ferric-reducing antioxidant power (FRAP) assays, employing Trolox as a standard. The performed in vitro antibacterial screening indicates a selective antibacterial activity against Gram-negative *K. pneumoniae* and *P. aeruginosa*, while no such activity is detected for Gram-negative *E. coli* and Gram-positive *S. aureus*.

Keywords: quaternary ammonium compound; Schiff base; NMR; SCXRD; DSC; antioxidant; antibacterial

Citation: Rusew, R.; Georgieva, M.; Kurteva, V.; Shivachev, B. Novel Quaternary Ammonium Aldimine Derivatives Featuring 3,4,5-Trimethoxy Phenyl Fragment: Synthesis, Crystal Structure and Evaluation of Antioxidant and Antibacterial Activity. *Crystals* **2024**, *14*, 486. https://doi.org/10.3390/cryst14060486

Academic Editors: Vasundara Srinivasan and Santosh Panjikar

Received: 29 April 2024
Revised: 16 May 2024
Accepted: 17 May 2024
Published: 22 May 2024

1. Introduction

The rise of antimicrobial resistance (AMR) poses a serious threat to global public health, rendering many existing antibacterial treatments ineffective against pathogenic bacteria [1]. The main factors that exacerbate this issue are the overuse and misuse of antibiotics in both human medicine and agriculture [2], combined with the dwindling pipeline of novel antimicrobial drugs [3,4]. Regardless of the significant progress in medical and chemical science, finding drugs with improved mechanisms of action towards novel bacterial targets has become progressively more difficult and costly [5–7]. Although the growing scientific interest in the exploration of alternative sources for antibiotic discovery, including natural products from diverse environments such as soil, marine organisms, and even human microbiota [8–10], the classical approach based on chemical alterations of existing biologically active molecular scaffolds is still relevant [11–13]. Suitable molecular scaffolds in this regard are Schiff bases and quaternary ammonium compounds (QACs). This is justified by their broad spectrum of biological properties but also by their simple and economical synthetic protocols, ease of purification and chemical versatility, facilitating the preparation of various derivatives.

Schiff bases are the products of a condensation reaction between an aromatic/aliphatic primary amine and an aromatic/aliphatic carbonyl compound, resulting in the formation of azomethine bond. The electronic environment around the azomethine bond, i.e., the presence of unpaired electrons on the nitrogen atom, plays a major role in defining the properties of Schiff bases, centered around their ability to form coordination complexes with metal ions [14,15]. Schiff bases and their metal complexes are applied as ligands in coordination [16] and analytical chemistry [17], as corrosion inhibitors for metals and alloys [18], as catalysts in organic synthesis [19,20], as photoluminescent materials [21,22] among others. Furthermore, Schiff bases and their metal complexes display diverse biological activities with application in medicinal chemistry, including antimicrobial [23–25], antifungal [26,27], anticancer [28,29], anti-inflammatory [30,31], antimalarial [32,33], antiviral [34,35], and antioxidant [36,37] properties.

Quaternary ammonium compounds (QACs) are obtained using a straightforward synthetic protocol involving the reaction of tertiary aromatic/aliphatic amines with alkyl/aryl halides in polar aprotic solvents, thus forming a hydrophilic positively charged nitrogen center (N^+, "head") and hydrophobic aliphatic/aromatic "tails". The amphiphilic nature of QACs contributes to their applications as cationic surfactants [38], phase-transfer catalysts [39], ionic liquids [40], corrosion inhibitors [41] and biological stains and dyes such as ethidium bromide [42], propidium iodide [43], crystal violet [44], etc. QACs possessing long aliphatic chains, such as benzalkonium, cetrimonium, and dequalinium, are commercial antiseptics and disinfectants. Other medical research areas reveal their antimalarial [45], anticancer [46,47], and antifungal [48,49] potential. Research in these areas aims to elucidate the mechanisms of action of QACs, optimize their pharmacological properties, and evaluate their efficacy and safety profiles (toxicity, cytotoxicity etc.)

In the context of antibiotic/antimicrobial research, the current study is focused on the merging of the characteristic molecular features of Schiff bases and QACs—the azomethine bond (–CH=N–) and the positively charged nitrogen center (N^+)—into a single molecule with the potential of unlocking improved biological effect. Moreover, all reported compounds feature the 3,4,5-trimethoxy phenyl (TMP) moiety, a commonly employed structural motif found in various organic compounds with diverse biological properties. TMP is found in Trimethoprim, an antibiotic used to treat urinary tract infections [50]. Trimetrexate, an analog of Trimethoprim, is used for the treatment of moderate-to-severe fungal infections [51], but it has also been investigated as a potential chemotherapy agent for the treatment of various cancers, including leukemia and lymphoma [52,53]. The TMP moiety is found in many natural alkaloids with important biological properties such as Podophyllotoxin, Colhicine, and Combretastatin A-4 (CA-4). Podophyllotoxin [54], derived from *Podophyllum peltatum*, exhibits antimitotic activity by interfering with microtubule function, making it useful in the treatment of certain skin conditions and as a precursor for semisynthetic anticancer drugs like etoposide and teniposide [55,56]. Colchicine is a plant-derived alkaloid inhibiting microtubule polymerization, which disrupts mitosis and inflammatory processes [57]. CA-4 is a stilbene derivative with potent antimitotic and antivascular properties [58]. It disrupts microtubule function and causes vascular shutdown, making it a promising candidate for cancer therapy, particularly in combination with other chemotherapeutic agents [59–61].

From the above, it is clear that the proposed combination of a Schiff base and a quaternary ammonium compound could provide beneficial synergism towards enhanced antimicrobial properties. The presence of a known biologically active fragments/moieties may further enhance the antimicrobial activity. Herein, we report the synthesis, characterization, and structural analysis of five novel quaternary ammonium aldimine derivatives, containing a TMP moiety, and evaluate their antioxidant and antibacterial properties.

2. Materials and Methods

2.1. Materials

All starting materials for the synthesis, purification and crystallization of the 4-pyridine carboxaldehyde (4-PCA) derivatives were purchased from Sigma Aldrich (Merck, Rahway, NJ, USA) or Alfa Aesar (Thermo Fisher Scientific, Waltham, MA, USA) and used without further purification. All reagents for the antioxidant activity assays, including 2-Diphenyl-1-pikrylhydrazyl (DPPH), 2,4,6-tris(2-pyridyl)-s-triazine (TPTZ), and 6-hydroxy-

2,5,7,8-tetramethylchromane-2-carboxilic acid (Trolox), were of analytical grade and were purchased from Sigma-Aldrich (Merck, USA).

2.2. General Synthesis Procedure

The quaternary ammonium aldimine derivatives were prepared by a two-step synthetic procedure featuring azomethine bond formation (–CH=N–) followed by quaternization of the pyridine *N*-atom with various aromatic α-bromo ketones (Scheme 1). The reaction conditions for the preparation of the aldimine derivative **2** were chosen according to a synthetic protocol described by Morales et al. [62]. In general, the procedure involves the addition of 4-pyridine carboxaldehyde (3 eq.) to a mixture of dichloromethane, 10 mol % pyrrolidine as catalyst, and 4Å molecular sieve. After the pre-mixing period (~10 min), 3,4,5-trimetoxyaniline (2.5 eq.) was added, and the resulting mixture was further stirred in closed vessel for 30 h at 40 °C. The end of the reaction was confirmed with thin-layer chromatography using Silica gel 60 F_{254} aluminum sheets as the stationary phase and a solution of ethyl acetate: hexane (3:1 *v*/*v*) as the mobile phase. The crude reaction mixture was filtered over a short pad of Celite® 545, the collected filtrate was vacuum-evaporated, and the obtained solid mass was recrystallized from dichloromethane resulting in large yellow block crystals (yield 85%). The quaternization of the pyridine *N*-atom of compound **2** was achieved in acetonitrile with five aromatic α-bromo ketones at 60 °C. The reaction completion was marked with the formation of yellow to orange colored microcrystalline precipitates (yields 65–77%) that were isolated by filtration and purified by washing with cold acetonitrile. The purity and the molecular structure of the studied compounds in solution were assessed with 1D (^{1}H- and ^{13}C) and 2D (NOESY, HSQC and HMBC) NMR techniques (Figures S1–S29) in DMSO-d_6, while the purity in a solid state was investigated by the comparative analysis of the diffracting patterns of the products and starting reagents obtained by powder and single-crystal X-ray diffraction experiments (Figures S42–S47).

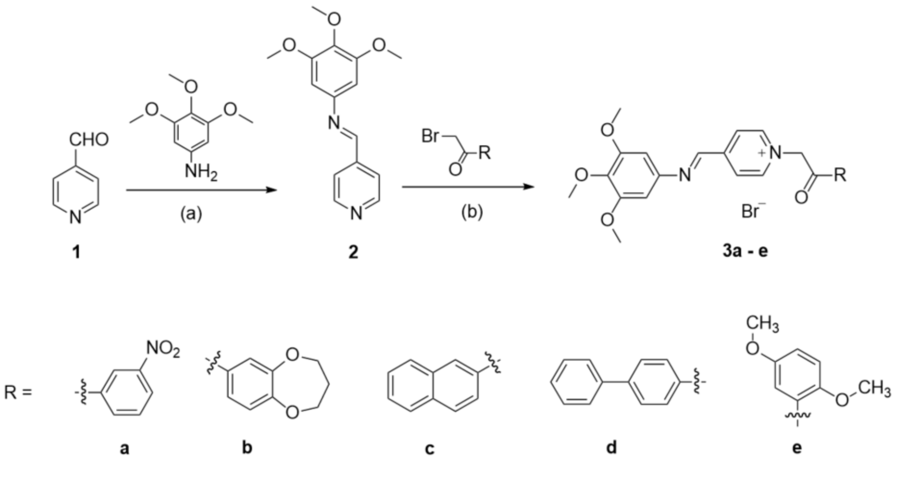

Scheme 1. General procedure for the synthesis of 4-pyridine carboxaldehyde analogues (**3a**–**e**): (a) 4-pyridin carboxaldehyde, 3,4,5-trimethoxyaniline, (Aldehyde: Amine—3 eq.:2.5 eq.), dichloromethane, 10 mol % pyrrolidine, 4Å molecular sieve, 40 °C, 30 h, reflux; (b) acetonitrile, 60 °C, 0.25–3 h, reflux.

2.2.1. Synthesis of 1-(Pyridin-4-yl)-N-(3,4,5-trimethoxyphenyl)methanimine (**2**)

4-pyridine carboxaldehyde (3 mmol, 283 µL, ρ = 1.137 g/cm^{3}), 3,4,5-trimethoxy aniline (2.5 mmol, 458 mg), 15 mL dichloromethane, 0.5 g 4Å molecular sieve, 10 mol % pyrrolidine, 40 °C, 30 h, reflux. Compound **2**: yield: 85%, Rf- ethyl acetate: hexane (3:1 *v*/*v*) 0.69; yellow block crystals (dichloromethane); mp 126–128 °C; FT-IR [63–65]: 2841 cm^{-1} (C–H stretching, O–CH_3), 1600 cm^{-1} (C=N stretching, imine), 1122 cm^{-1} (C–O stretching, O–CH_3); ^{1}H NMR (DMSO-d_6, 400 MHz) δ 3.688 (s, 3H, OMe-4′), 3.839 (s, 6H, OMe-3′ and OMe-5′), 6.729 (s, 2H, CH-2′ and CH-6′), 7.80–7.87 (m, 2H, CH-3 and CH-5), 8.72–8.79 (m, 3H, CH=N, CH-2 and CH-6). ^{13}C NMR (DMSO-d_6, 101 MHz) δ 56.43 (C-methoxy-3′and 5′) 60.60

(C-methoxy-4′), 99.57 (C-2′ and C-6′), 122.57 (C-3 and C-5), 137.11 (Cq-4′), 143.02 (Cq-4), 146.64 (Cq-1′), 150.94 (C-2 and C-6), 153.73 (Cq-3′ and Cq-5′), 158.84 (CH=N); HR-MS (ESI$^+$) *m*/*z* calcd. for $C_{15}H_{17}N_2O_3^+$ [M + H]$^+$ 273.1234, found 273.1230, Δ = −0.4 mDa.

2.2.2. Synthesis of 1-(2-(3-Nitrophenyl)-2-oxoethyl)-4-(((3,4,5-trimethoxyphenyl)imino)methyl)pyridin-1-ium bromide (**3a**)

Compound **2** (0.35 mmol, 96 mg), 2-Bromo-3′-nitroacetophenone (0.40 mmol, 98 mg), 5 mL acetonitrile, 60 °C, 0.25 h, reflux. Compound **3a**: yield 71%, orange block crystals (methanol/acetone); decompose without melting at 216–218 °C; FT-IR [63–65]: 2838 cm^{-1} (C–H stretching, O–CH_3), 1705 cm^{-1} (C=O stretching, conjugated ketone), 1645 cm^{-1} (C=N stretching, imine), 1131 cm^{-1} (C–O stretching, O–CH_3); ^{1}H NMR (DMSO-d_6, 400 MHz) δ 3.736 (s, 3H, OMe-4′), 3.879 (s, 6H, OMe-3′ and OMe-5′), 6.600 (s, 2H, CH_2–C=O), 6.916 (s, 2H, CH-2′ and CH-6′), 7.999 (t, *J* = 8.0 Hz, 1H, CH-5″), 8.499 (ddd, 1H, *J* = 7.8, 1.7 Hz, 1.1 Hz, CH-6′), 8.62–8.68 (m, 3H, CH-4″, CH-3 and CH-5), 8.785 (t, 1H, *J* = 2 Hz, CH-2″), 9.082 (t, *J* = 3.4 Hz, 3H, CH=N, CH-2 and CH-6). ^{13}C NMR (DMSO-d_6, 101 MHz) δ 56.58 (C-methoxy-3′and 5′), 60.68 (C-methoxy-4′), 66.72 (CH_2–C=O), 100.56 (C-2′ and C-6′), 123.09 (C-2″), 126.11 (C-3 and C-5), 129.19 (C-4″), 131.57 (C-5″), 134.86 (C-6″), 135.44 (Cq-1″), 138.60 (Cq-4′), 145.31 (Cq-1′), 147.54 (C-2 and C-6), 148.60 (Cq-3″), 150.92 (Cq-4), 153.84 (Cq-3′ and Cq-5′), 155.65 (CH=N), 190.21 (C=O). HR-MS (ESI$^+$) *m*/*z* calcd. for $C_{23}H_{22}N_3O_6^+$ 436.1503, found 436.1499, Δ = −0.4 mDa; HR-MS (ESI$^-$) *m*/*z* calcd. for $^{79}Br^-$ 78.9178, found 78.9176, Δ = −0.2 mDa.

2.2.3. Synthesis of 1-(2-(3,4-Dihydro-2H-benzo[b][1,4]dioxepin-7-yl)-2-oxoethyl)-4-(((3,4,5-trimethoxyphenyl)imino)methyl)pyridin-1-ium bromide (**3b**)

Compound **2** (0.35 mmol, 96 mg), 7-Bromoacethyl-3,4-dihydro-1,5-benzodioxepin (0.40 mmol, 109 mg), 5 mL acetonitrile, 60 °C, 3h, reflux. Compound **3b**: yield 69%, orange microcrystalline powder (acetonitrile); decompose without melting at 250–252 °C; FT-IR [63–65]: 2837 cm^{-1} (C-H stretching, O–CH_3), 1687 cm^{-1} (C=O stretching, conjugated ketone), 1642 cm^{-1} (C=N, stretching, imine), 1125 cm^{-1} (C–O stretching, O–CH_3); ^{1}H NMR (DMSO-d_6, 400 MHz) δ 2.219 (p, 2H, *J* = 5.7 Hz, CH_2-8″), 3.733 (s, 3H, OMe-4′), 3.877 (s, 6H, OMe-3′ and OMe-5′), 4.264 (t, 2H, *J* = 5.8 Hz, CH_2-7″), 4.329 (t, 2H, *J* = 5.6 Hz, CH_2-9″), 6.442 (s, 2H, CH_2–C=O), 6.907 (s, 2H, CH-2′ and CH-6′), 7.209 (d, 1H, *J* = 8.4 Hz, CH-3″), 7.60–7.73 (m, 2H, CH-6″, CH-2″), 8.58–8.65 (m, 2H, CH-3 and CH-5), 9.04–9.11 (m, 3H, CH-2 and CH-6, CH=N). ^{13}C NMR (DMSO-d_6, 101 MHz) δ 30.93 (C-8″), 56.57 (C-methoxy-3′ and C-methoxy-5′), 60.71 (C-methoxy-4′), 66.37 (CH_2–C=O), 70.98 (C-9″), 71.07 (C-7″), 100.54 (C-2′ and C-6′), 122.37 (C-6″), 122.45 (C-3″), 124.65 (C-2″), 126.00 (C-3 and C-5), 129.10 (Cq-1″), 138.58 (Cq-4′), 145.31 (Cq-1′), 147.49 (C-2 and C-6), 150.70 (Cq-4), 150.99 (Cq-5″), 153.84 (Cq-3′and Cq-5′), 155.64 (CH=N), 156.80 (Cq-4″), 189.48 (C=O). HR-MS (ESI$^+$) *m*/*z* calcd. for $C_{26}H_{27}N_2O_6^+$ 463.1864, found 463.1859, Δ = −0.5 mDa; HR-MS (ESI$^-$) *m*/*z* calcd. for $^{79}Br^-$ 78.9178, found 78.9176, Δ = −0.2 mDa.

2.2.4. Synthesis of 1-(2-(Naphthalen-2-yl)-2-oxoethyl)-4-(((3,4,5-trimethoxyphenyl)imino)methyl)pyridin-1-ium bromide (**3c**)

Compound **2** (0.35 mmol, 96 mg), 2-(Bromoacetyl) naphthalene (0.40 mmol, 100 mg), 5 mL acetonitrile, 60 °C, 0.5 h, reflux. Compound **3c**: yield 65%, orange plate crystals (methanol/acetone); decompose without melting at 231–233 °C; FT-IR [63–65]: 2835 cm^{-1} (C–H stretching, O–CH_3), 1687 cm^{-1} (C=O stretching, conjugated ketone), 1640 cm^{-1} (C=N, stretching, imine), 1133 cm^{-1} (C–O stretching, O–CH_3); ^{1}H NMR (DMSO-d_6, 400 MHz) δ 3.738 (s, 3H, OMe-4′), 3.883 (s, 6H, OMe-3′ and OMe-5′), 6.653 (s, 2H, CH_2–C=O), 6.920 (s, 2H, CH-2′ and CH-6′), 7.755 (dddd, 2H, *J* = 21.1 Hz, 8.2 Hz, 6.9 Hz, 1.4 Hz, CH-7″ and CH-6″), 8.081 (m, 2H, CH-3″ and CH-5″), 8.179 (d, 1H, *J* = 8.8 Hz, CH-4″), 8.247 (d, 1H, *J* = 7.4 Hz, CH-8″), 8.64–8.68 (m, 2H, CH-3 and CH-5), 8.850 (d, 1H, *J* = 1.8 Hz, CH-1″), 9.077 (s, 1H, CH=N), 9.15–9.19 (m, 2H, CH-2 and CH-6). ^{13}C NMR (DMSO-d_6, 101 MHz) δ 56.59 (C-methoxy-3′ and 5′), 60.72 (C-methoxy-4′), 66.69 (CH_2–C=O), 100.57 (C-2′ and C-6′), 123.73 (C-3″), 126.05 (C-3 and C-5), 127.99 (C-7″), 128.42 (C-5″), 129.35 (C-4″), 129.98 (C-6″), 130.22

(C-8″), 131.18 (C-1″), 131.36 (Cq-2″), 132.49 (Cq-8a″), 136.11 (Cq-4a″), 138.58 (Cq-4′), 145.34 (Cq-1′), 147.58 (C-2 and C-6), 150.77 (Cq-4), 153.85 (Cq-3′ and Cq-5′), 155.68 (CH=N), 191.09 (C=O). HR-MS (ESI$^+$) m/z calcd. for $C_{27}H_{25}N_2O_4{}^+$ 441.1809, found 441.1808, Δ = −0.1 mDa; HR-MS (ESI$^-$) m/z calcd. for $^{79}Br^-$ 78.9178, found 78.9176, Δ = −0.2 mDa.

2.2.5. Synthesis of 1-(2-([1,1′-Biphenyl]-4-yl)-2-oxoethyl)-4-(((3,4,5-trimethoxyphenyl)imino)methyl)pyridin-1-ium bromide (**3d**)

Compound **2** (0.35 mmol, 96 mg), 2-Bromo-4′-phenylacetophenone (0.40 mmol, 110 mg), 5 mL acetonitrile, 60 °C, 0.5 h, reflux. Compound **3d**: yield 74%, orange block crystals (methanol/acetone); decompose without melting at 218–221 °C; FT-IR [63–65]: 2837 cm^{-1} (C–H stretching, O–CH_3), 1688 cm^{-1} (C=O stretching, conjugated ketone), 1641 cm^{-1} (C=N, stretching, imine), 1127 cm^{-1} (C–O stretching, O–CH_3); ^{1}H NMR (DMSO-d_6, 400 MHz) δ 3.737 (s, 3H, OMe-4′), 3.881 (s, 6H, OMe-3′ and OMe-5′), 6.555(s, 2H, CH_2–C=O), 6.918 (s, 2H, CH-2′ and CH-6′), 7.46–7.51 (m, 1H, CH-4‴), 7.54–7.59 (d, 2H, CH-3‴ and CH-5‴), 7.82–7.86 (m, 2H, CH-2‴ and CH-6‴), 7.97–8.06 (m, 2H, CH-3″ and CH-5″), 8.16–8.20 (m, 2H, CH-2″ and CH-6″), 8.64–8.67 (m, 2H, CH-3 and CH-5), 9.072 (s, 1H, CH=N), 9.09–9.12 (m, 2H, CH-2 and CH-6). ^{13}C NMR (DMSO-d_6, 101 MHz) δ 56.58 (C-methoxy-3′ and 5′), 60.72 (C-methoxy-4′), 66.62 (CH_2–C=O), 100.55 (C-2′ and C-6′), 126.02 (C-3 and C-5), 127.65 (C-2‴ and C-6‴), 127.71 (C-3″ and C-5″), 129.29 (C-4‴), 129.54 (C-2″ and C-6″), 129.69 (C-3‴ and C-5‴), 132.84 (Cq-1″), 138.58 (Cq-4′), 138.95 (Cq-1‴), 145.33 (Cq-1′), 146.42 (Cq-4″), 147.55 (C-2 and C-6), 150.75 (Cq-4), 153.85 (Cq-3′ and Cq-5′), 155.67 (CH=N), 190.73 (C=O); HR-MS (ESI$^+$) m/z calcd. for $C_{29}H_{27}N_2O_4{}^+$ 467.1965, found 467.1965, Δ = 0.0 mDa; HR-MS (ESI$^-$) m/z calcd. for $^{79}Br^-$ 78.9178, found 78.9176, Δ = −0.2 mDa.

2.2.6. Synthesis of 1-(2-(2,5-Dimethoxyphenyl)-2-oxoethyl)-4-(((3,4,5-trimethoxyphenyl)imino)methyl)pyridin-1-ium bromide (**3e**)

Compound **2** (0.35 mmol, 96 mg), 2-Bromo-2′, 5′-dimetoxyacetophenone (0.40 mmol, 104 mg), 5 mL acetonitrile, 60 °C, 2h, reflux. Compound **3e**: yield 77%, light yellow microcrystalline powder (acetonitrile); decompose without melting at 205–207 °C; FT-IR [63–65]: 2834 cm^{-1} (C–H stretching, O–CH_3), 1673 cm^{-1} (C=O stretching, conjugated ketone), 1645 cm^{-1} (C=N, stretching, imine), 1124 cm^{-1} (C–O stretching, O–CH_3); ^{1}H NMR (DMSO-d_6, 400 MHz) δ 3.731 (s, 3H, OMe-4′), 3.773 (s, 3H, OMe-5″), 3.874 (s, 6H, OMe-3′ and OMe-5′), 4.021 (s, 3H, OMe-2″), 6.259 (s, 2H, CH_2–C=O), 6.903 (s, 2H, CH-2′ and CH-6′), 7.31–7.40 (m, 3H, CH-4″ and CH-3″, CH-6″), 8.58–8.62 (m, 2H, CH-3 and CH-5), 9.040 (s, 1H, CH=N), 9.07–9.10 (m, 2H, CH-2 and CH-6). ^{13}C NMR (DMSO-d_6, 101 MHz) δ 56.17 (C-metoxy-5″), 56.57 (C-metoxy-3′ and 5′), 57.20 (C-metoxy-2″), 60.71 (C-metoxy-4′), 70.27 (CH_2–C=O), 100.51 (C-2′ and C-6′), 113.86 (C-6″), 115.27 (C-4″), 123.31 (C-3″), 123.62 (Cq-1″), 125.76 (C-3 and C-5), 138.53 (Cq-4′), 145.35 (Cq-1′), 147.49 (C-2 and C-6), 150.55 (Cq-4), 153.66 (Cq-5″), 153.83 (Cq-3′ and Cq-5′), 155.09 (Cq-2″), 155.70 (CH=N), 190.27 (C=O); HR-MS (ESI$^+$) m/z calcd. for $C_{25}H_{27}N_2O_6{}^+$ 451.1864, found 451.1859, Δ = −0.5 mDa; HR-MS (ESI$^-$) m/z calcd. for $^{79}Br^-$ 78.9178, found 78.9177, Δ = −0.1 mDa.

2.3. Characterization Methods

2.3.1. Single-Crystal X-ray Diffraction (SCXRD) Analysis

Suitable single crystals of compounds **2**, **3a**, **3c** and **3d** (dimensions~0.3 × 0.2 × 0.1 mm^3, without visual cracks and adhesions) were mounted on nylon loops using viscous cryoprotectant (Paratone® N). Diffraction data were collected at 290 K on a Bruker D8 Venture diffractometer equipped with an *IμS* micro-focus sealed Mo X-ray source (λ = 0.71073 Å) and PHOTON II CPAD detector. APEX4 ver. 2021.10-0 [66] was used as the data acquisition and processing software. Data integration and scaling were carried out with Bruker SAINT ver. 8.40B [67], and a multi-scan absorption correction was performed with SADABS ver. 2016/2 [67]. The crystal structures of **2**, **3a**, **3c** and **3d** were solved with ShelxT ver. 2018/2 (intrinsic phasing method [68]), the structural model was refined with ShelxL ver. 2019/1 (full-matrix least-squares method on F^2 [69]), and program packages included in Olex2 ver. 1.5 [70] graphical interface. All heteroatoms (C, O, N and Br) were located from the electron density maps and were anisotropically refined. Hydrogen atoms were placed in calculated positions and refined using the following riding model: Ueq = 1.2 for C-$H_{aromatic}$ = 0.93 Å and C-$H_{methylenic}$ = 0.97 Å and Ueq = 1.5 for C-H_{methyl} = 0.96 Å. The molecules of **2**, **3a**, **3c** and **3d** present in the asymmetric unit (ASU) were visualized using ORTEP-3 ver. 2020.1 software [71]. Illustrations concerning the detected intra- and inter-molecular interactions and crystal packing were prepared using Mercury ver. 4.0 [72] software. Important crystal data and structure refinement parameters are summarized in Table S1. Values for bond lengths, bond angles, and torsion angles obtained from the SCXRD are given in Tables S2–S5, Tables S6–S9 and Tables S10–S13, respectively. Data concerning the detected halogen and hydrogen bonding interactions and short contacts for the crystal structures are given in Tables S14–S17, respectively. Complete crystallographic data for the reported structures of **2**, **3a**, **3c** and **3d** were deposited in CIF format with the Cambridge Crystallographic Data Centre (ref. codes 2333781–2333784). These data can be obtained free of charge via www.ccdc.cam.ac.uk/structures (accessed on 19 February 2024).

2.3.2. Powder X-ray Diffraction (PXRD) Analysis

Powder X-ray diffraction analysis was conducted using an Empyrean Powder X-ray diffractometer (Malvern Panalytical, Almelo, The Netherlands) equipped with a copper X-ray source (λ = 1.5406 Å) and a PIXcel3D area detector. The diffraction patterns of compounds 2, **3a–e** were collected in the 2–50° 2Theta range using the following operation conditions: 40 kV/30 mA, step size of 0.013°, and rotation speed of 15 rpm. The powder patterns of the bulk microcrystalline products (**2**, **3a–e**) were compared with the powder patterns of the starting reagents and those generated from the SCXRD analysis, thus confirming the presence of desired/undesired crystalline/amorphous phases (Figures S42–S47). Data Viewer ver. 1.9a software (Malvern Panalytical, Almelo, The Netherlands) was used for visualization of the powder patterns.

2.3.3. Nuclear Magnetic Resonance (NMR) Spectroscopy

The NMR spectra of compounds **2**, **3a–e** were recorded on a Bruker Avance NEO 400 spectrometer (Rheinstetten, Germany) in DMSO-d6. The one-dimensional (1D) ^{1}H and ^{13}C NMR measurements were performed at 400 MHz and 101 MHz, respectively. The chemical shifts were quoted in parts per million (ppm) in δ-values against the solvent peak at 2.5 ppm, and the spin–spin coupling constants were calculated in Hz. Spin multiplicities are given as singlet (s), doublet (d), doublet of doublets (dd), doublet of doublets of doublets (ddd), triplet (t), pentet (p) and multiplet (m). Signals were assigned using a combination of two-dimensional (2D) NOESY, HSQC, and HMBC techniques. The spectra were processed with Topspin ver. 3.6.3. program.

2.3.4. Differential Scanning Calorimetry (DSC)

Differential scanning calorimetry analysis was performed on Discovery DSC 250 (TA instruments, New Castle, DE, USA). Samples weighing between 1 and 3 mg were heated in closed aluminum pans from 30 to 270 °C (heating rate 10 $°C \cdot min^{-1}$) in a dynamic nitrogen atmosphere (flow rate 20 $mL \cdot min^{-1}$). The melting point was determined from DSC analysis only for compound **2** as compounds **3a–e** decompose without melting.

2.3.5. Fourier-Transform Infrared (FT-IR) Spectroscopy

The FT-IR spectra of compounds **2**, **3a–e** were collected on a Tensor 37 (Bruker, Berlin, Germany) spectrometer in the region of 4000–400 cm^{-1} (128 scans) using KBr pellets (sample: KBr–1:50 *w*/*w*).

2.3.6. High-Resolution Mass Spectrometry (HR-MS)

The mass spectra were recorded using a Q Exactive Plus Hybrid Quadrupole-Orbitrap Mass Spectrometer from Thermo Scientific (HESI HRMS) in both positive and negative modes. The spectra were processed with Thermo Scientific FreeStyle program ver. 1.8 SP1 (Thermo Fisher Scientific Inc., Waltham, MA, USA).

2.3.7. Antioxidative Activity Assays

The antioxidant properties of compounds **2**, **3a**–**e** were evaluated spectrophotometrically using DPPH radical scavenging and ferric-reducing antioxidant power (FRAP) assays. The measurements were performed on Varian Cary 100 UV-Vis spectrophotometer (Agilent Technologies, Santa Clara, CA, USA). All analyses were carried out at least in four replicates.

The DPPH assay was conducted according to Brand-Williams et al. [73]. Briefly, 3 mL of DPPH stock solution (2.4 mg DPPH in 100 mL methanol) was mixed with 0.4 mL methanol solution of compounds **2**, **3a**–**e** (0.1 mg/mL). The absorbance of the reaction mixture was measured at 517 nm after 20 min of incubation in the dark at room temperature. Methanol was used as blank and DPPH/methanol solution as a negative control.

The FRAP assay was carried out according to the method of Benzie and Strain [74]. The FRAP reagent was prepared by mixing 25 mL acetate buffer (300 mM, pH 3.6), 2.5 mL TPTZ solution (10 mM in HCl (40mM)), and 2.5 mL $FeCl_3$ solution (20 mM in 10 mL dist. water). For the experiment, 3 mL of the stock FRAP solution was mixed with 0.4 mL methanol solution of compounds **2**, **3a**–**e** (0.1 mg/mL). The absorbance of the reaction mixture was measured at 593 nm after 4 min of incubation in the dark at room temperature. FRAP reagent solution was used as blank and negative control. Calibration curves for both assays were obtained using Trolox standards in the range of 50–250 µmol/L, and the antioxidant activity (i.e., scavenging activity or ferric-reducing power) values of **2**, **3a**–**e** were expressed as mmol Trolox equivalents (TE) per g of each sample using the following equation:

$$\text{Antioxidant activity}\left(\text{mMTEg}^{-1}\right) = \frac{c * V * DF}{m} \tag{1}$$

where c is the Trolox concentration (mM/L) of the corresponding standard curve, V is the sample volume (L), DF is the dilution factor (DF = 1), and m is the weight of the sample dry matter (g).

2.3.8. Bacterial Susceptibility Testing—Disk-Diffusion and Broth Microdilution Methods

The susceptibility of four bacterial strains—*Klebsiella pneumoniae*, *Pseudomonas aeruginosa*, *Escherichia coli*, and *Staphylococcus aureus* (obtained from the National Bank for Industrial Microorganisms and Cell Cultures, Sofia, Bulgaria, NBIMCC №: 3670, 644(ATCC 10145), 3397 and 509, respectively)—against the synthesized compounds **2**, **3a**–**e** was assessed using the Kirby–Bauer disk-diffusion method. The bacterial suspensions were grown overnight (12–15 h) in liquid growth medium (Lysogeny broth) and then diluted to concentrations of ~1.10^7–1.10^8 cfu mL^{-1} (Log phase of growth) corresponding to optical density of ~0.1 measured at 600 nm (~0.5 McFarland standard). Freshly autoclaved agar containing Mueller–Hinton growth medium was transferred into sterile Petri dishes and then allowed to cool down and solidify for 6h. Solutions of compounds **2**, **3a**–**e** and the reference antibiotic kanamycin with concentrations of 1 mg/mL in 4% DMSO were prepared. A volume of 30 µL (corresponding to 30 µg of the test compounds and kanamycin) was pipetted onto sterile filter paper discs of 6 mm diameter, and then the discs were left to dry for 12 h. The solid agar medium was inoculated with small amounts (0.1 mL) of each bacterial suspension, spread uniformly across the surface using cell spreader. Next, the paper disks impregnated with the studied compounds were placed on the surface of the inoculated agar medium. Finally, the plates were incubated at 37 °C for 12 to 18 h. The diameters of the areas around the discs with no visible growth were measured using ImageJ ver. 1.52a software [75].

All substances tested by the disk diffusion method and showing antibacterial properties were further investigated using the broth microdilution (BMD) method to determine the minimum inhibitory concentration (MIC). The bacterial suspensions were grown overnight

(12–15 h) in Mueller–Hinton broth (HMB) and then diluted to concentrations of ~1.10^6 cfu mL^{-1}. Next, 100 μL of the stock solution (1 mg/mL) of test compounds was placed in the first well of 96-well microtiter plates. In the next 9 wells, 50 μL of HMB was placed. Then, a serial dilution was performed for wells 1–10. After the serial dilution was performed in each well, 50 μL of the ~1.10^6 cfu mL^{-1} bacterial suspensions was added. The final concentration range for the test compounds was from 500 to 0.98 μg/mL. The last two wells were the growth (bacterial suspension only) and sterile controls (HMB only). After incubation for 18 h, the absorbance at 600 nm of each well was measured using a microplate reader (ELx800, Biotek, Winooski, VT, USA). The experiments were conducted in triplicate. From the absorbance values obtained, a graph was plotted reflecting the survival rate (% of viability) of the microorganisms at a given concentration of the substance (μg/mL). The MIC values were deduced from the data.

3. Results and Discussion

3.1. Synthesis

The title quaternary ammonium aldimines (**3a**–**3e**) were prepared by an easy two-step synthetic procedure featuring an initial condensation reaction between 4-pyridinecarboxaldehyde (4-PCA) and 3,4,5-trimetoxyaniline for the preparation of aldimine **2**, followed by a quaternization reaction with various aromatic α-bromo ketones.

At first, the condensation reaction for the preparation of aldimine **2** was conducted in absolute ethanol in the presence of a catalytic amount of glacial acetic acid. However, due to the reversible nature of the aldimine formation (i.e., the possibility for the hydrolysis of the product in acidic conditions), the condensation reaction between the employed 4-pyridinecarboxaldehyde and 3,4,5-trimetoxyaniline was never “complete”, even after prolonged reaction times, elevated temperatures and variations in the quantity of the starting reagents. In order to shift the equilibrium towards the desired product **2**, a couple of modifications to the reaction conditions were made following a procedure described by Morales et al. [62]. The ethanol was replaced with the water-immiscible dichloromethane, small amounts of the 4Å molecular sieve were used in order to absorb the produced water and also pyrrolidine was employed as catalyst. According to these authors [62], the addition of catalytic amounts of pyrrolidine (usually 10 mol%) is required for the formation of an intermediate aldehyde–pyrrolidine product that is more reactive towards the employed amine. Although the detection of this intermediate product was not part of our study, evidence for its formation can be observed in the color change of the 4-PCA—pyrrolidine mixture (before the addition of the amine) from colorless to light yellow. Furthermore, it was found out that the reaction works very well when a slight excess of the starting 4-pyridinecarboxaldehyde (~20%) is employed, resulting in the depletion of the starting amine after 30 h of stirring at 40 °C. The employed post-synthetic procedure featuring filtration over a short pad of Celite® 545 (to remove molecular sieve and pyrrolidine catalyst), vacuum evaporation (to remove the excess of the liquid 4-PCA) and recrystallization from dichloromethane achieved compound **2** in 85% yield.

As next step, the pyridine *N* atom of **2** was involved in a quaternization reaction with various aromatic α-bromoketones. According to the literature, the quaternization process is best described as bimolecular nucleophilic substitution (S_N2). As such, the reaction rate of the quaternization process is favored by several factors, including the use of polar aprotic solvents as reaction media, lack of steric hindrance in the nucleophile and substrate molecules and the presence of a labile leaving group in the substrate [76–78]. Aromatic α-bromoketones, acting as substrate molecules, were chosen as alkylating agents due to their high reactivity, owing to the presence of the electron accepting carbonyl group (C=O), which favors the cleavage of the Br–CH_2 bond, and thus the easier attack of the nucleophile molecule (the *p*-substituted pyridine in **2**). It was found that the quaternization of **2** is best achieved in the polar aprotic acetonitrile as it offers good solubility of the starting reagents–**2** and aromatic α-bromoketones, while the obtained products **3a**–**3e** are insoluble. Thus, the purification and isolation of the products was reduced only to filtration and several washes with cold acetonitrile. The duration of the reaction varied from 15 min to 3 h as a function of the R-substituents present in the α-bromo ketones (reaction time increases in the following order of R-substituents: a < c ≡ d < e < b, Scheme 1). Finally, the reaction may be performed under an inert atmosphere (argon or nitrogen) and in dry reaction media to avoid the hydrolysis of the α-bromo ketones and/or the aldimine product.

As a result of the above considerations, one aldimine (**2**) and five quaternary ammonium aldimines (**3a**–**3e**) were obtained in good yields and their purity and molecular structures were assessed using NMR spectroscopy and powder X-ray diffraction techniques.

3.2. Crystal Structure Solution and Refinement

Yellow (**2**) and orange (**3a**, **3c** and **3d**) plate-(**3c**) or block (**2**, **3a** and **3d**)-shaped crystals were obtained by slow evaporation from hot dichloromethane (**2**) or methanol/acetone (**3a**, **3c** and **3d**) solutions. The studied compounds crystallize in the triclinic *P*-1 (**3d**), the monoclinic *C*2/*c* (**2** and **3c**), and the orthorhombic *Pbca* (**3a**) space groups with one molecule present in the asymmetric unit (ASU, Z′ = 1) and eight (**2**, **3a** and **3c**) or two (**3d**) molecules contained within the unit cell (Z = 8 or 2). The ORTEP view [71] of the molecules of compounds **2**, **3a**, **3c** and **3d** present in the ASU, with appropriate labeling and color scheme, are shown on Figure 1.

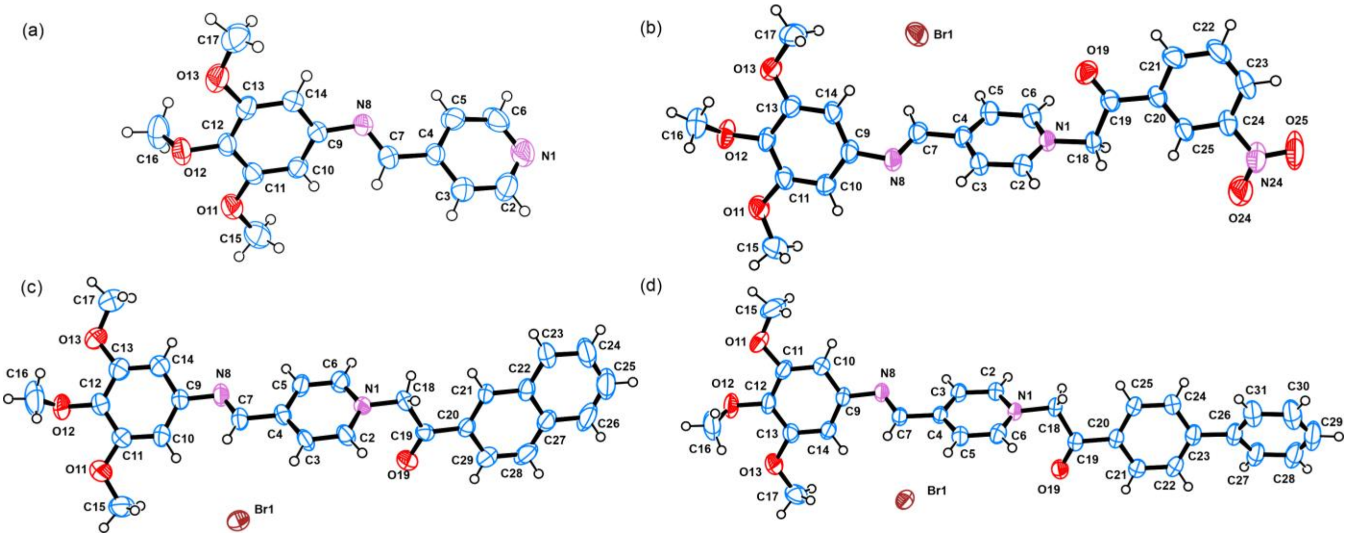

Figure 1. ORTEP view [71] of the molecules present in the ASU of the crystal structures of **2** (**a**), **3a** (**b**), **3c** (**c**) and **3d** (**d**) with appropriate labeling and color schemes. The atomic displacement parameters are given at 50% probability level and the hydrogen atoms as spheres with arbitrary radii.

The reported aldimine (**2**) and quaternary ammonium aldimine (**3a**, **3c** and **3d**) derivatives can be described as common in the build-up of all structures, which is caused by pyridine and 3,4,5-trimethoxy phenyl fragments, as well as aromatic substituents (Ar) introduced and employed in the quaternization process of α-bromo ketones (3-$NO_2C_6H_4$ for **3a**, naphthyl for **3c**, and biphenyl for **3d**). The pyridine fragment in all compounds is relatively planar with calculated RMSD values between 0.005 Å (for **3c**) and 0.008 Å (**3a**). The same is valid for the aromatic substituents 3-$NO_2C_6H_4$ (0.033 Å, **3a**), naphthyl (0.018 Å, **3c**), and biphenyl (0.010 Å/0.004 Å, **3d**). The phenyl part of the 3,4,5-trimetoxyphenyl fragment is also planar with RMSD variations between 0.005 Å (**3a**) and 0.016 Å (**3d**). However, considerable deviations from planarity are observed when the methoxy groups (O–CH_3) are taken into account with RMSD from 0.247 Å (**3a**) to 0.287 Å (**2**). The presence of azomethine (–CH=N–) and 2-oxoethyl (–CH_2–C(=O)–) bridging groups between the respective pyridine/3,4,5-trimethoxyphenyl and pyridine/Ar moieties contributes to the overall conformation flexibility of the molecules, confirmed by measuring the plane-to-plane twist and plane-to-plane fold angles. For example, the values for the pyridine/3,4,5-

trimethoxyphenyl twist and fold angles vary greatly between 30.0° (**3c**) and 136.80° (**2**) and between 3.4° (**2c**) and 178.09° (**2**), respectively. On the other hand, the twist and fold angles for pyridine/Ar fragments vary in close ranges between 113.87° (**3a**) and 120.10° (**2**) and between 18.08° (**3d**) and 30.5° (**3a**), suggesting more conservative geometry. Additional flexibility is observed for the biphenyl fragment in **3d** with twist and fold angles between the two phenyl rings of 34.15° and 8.11°, respectively. The conformation flexibility of compounds **2**, **3a**, **3c** and **3d** is clearly seen by overlaying the molecules present in the ASU by their common pyridine fragment (Figure 2).

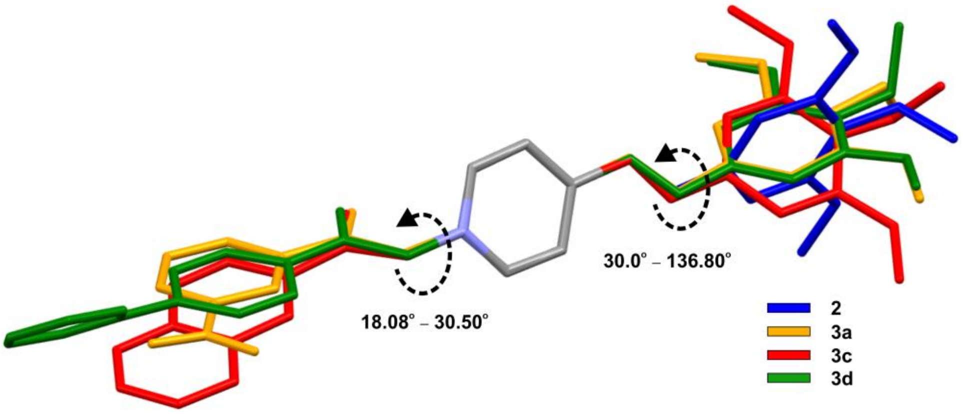

Figure 2. Overlay of the molecules of **2**, **3a**, **3c** and **3d** present in the ASU according to their common pyridine fragment, emphasizing the rotational flexibility of the molecules. Hydrogen atoms are omitted for clarity.

A close inspection of the molecular features of compounds **2**, **3a**, **3c** and **3d** reveals the presence of strong proton acceptors like functional groups of C=O (for **3a**, **3c** and **3d**) and NO_2 (for **3a**), moderately strong acceptors such as O–CH_3, and the azomethine group (–CH=N–), which can act as both a proton donor and acceptor, thus underlining the possibility of hydrogen bonding interactions. However, only weak interactions (considered short contacts) were detected between the C=O groups and the N-atoms from the pyridine ring and the azomethine group, different methyl, and methylene and aromatic CH groups (Figure S48, Tables S14–S17). On the other hand, the presence of a bromine anion and aromatic conjugated rings favors the possibility of the formation of halogen bonding, additional short contacts, and π-π stacking interactions. Indeed, the analysis of the three-dimensional packing of the molecules of **3a**, **3c** and **3d** reveals that the crystal structures are stabilized by a plethora of intermolecular halogen bonding interactions and short contacts of $C–H_{methylenic}$…Br and $C–H_{aromatic}$…Br types with H…Br distances between 2.73 and 3.07 Å (Figure S48, Tables S14–S17). Moreover, the methoxy groups in **2** and **3a** are involved in specific weak C–H…O interactions with the aromatic and methylene CH groups (in **2**) and with the aromatic CH groups (in **3a)** producing $R_2^2(9)$ and $R_2^2(8)$ motifs, respectively ([79,80], Figure 3a,b). Furthermore, these C–H…O interactions contribute to the specific three dimensional *zigzag* layering of the molecules projected along the *b* axis (for **2**, Figure 3a) and along the *c* axis (for **3a**, Figure 3b). In addition, one of the methoxy groups in **3a** is also involved in an intermolecular C–H…N interaction (namely C17-H17A…N8), with the imine *N* atom producing $C_1^1(8)$ chains in the direction of the *b* axis. Finally, staggered π-π stacking interactions are detected between the nitrobenzene/3,4,5-trimethoxy phenyl rings for **3a** and between the phenyl (C20-C21-C22-C23-C24-C25)/3,4,5-trimethoxy phenyl rings for **3d**. The stacking rings in **3a** and **3d** have mean plane angles of 7.574° and 6.828°, centroid to centroid distances of 3.719 Å and 3.842 Å, and shift distances of the centroids—1.090 Å and 1.567 Å, respectively.

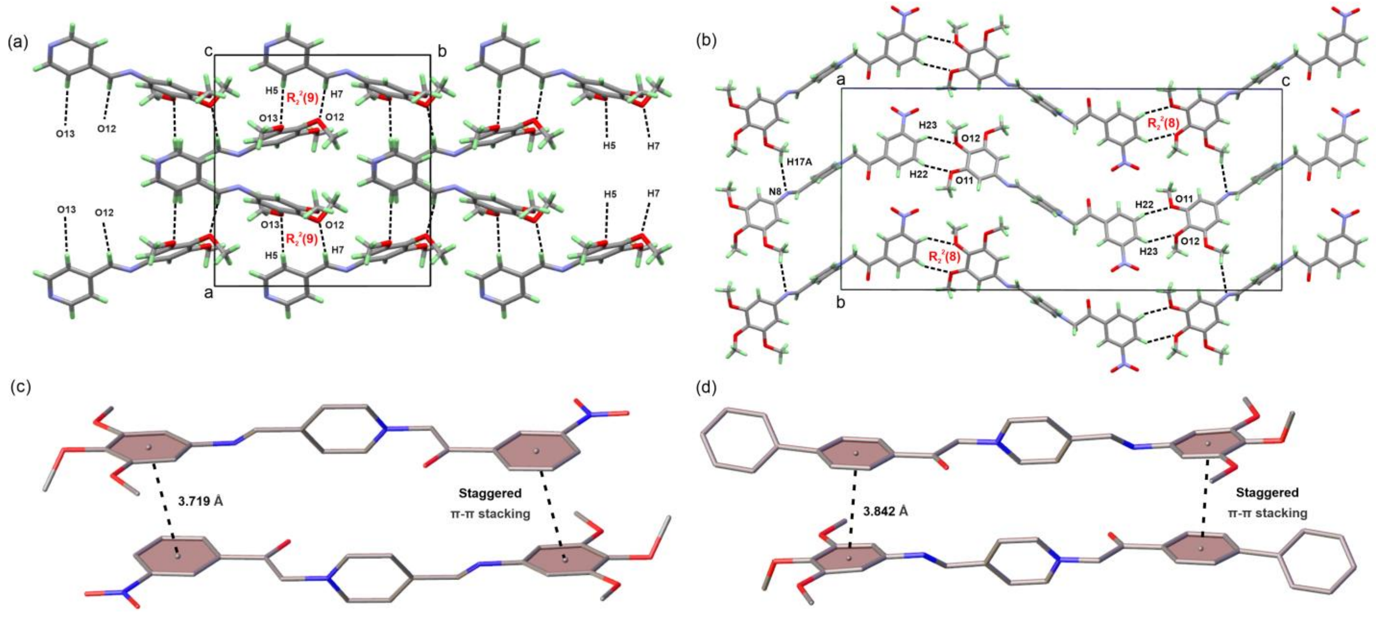

Figure 3. Representation of the crystal packing of the molecules of **2** (**a**) and **3a** (**b**), revealing specific C–H. . .O interactions and forming $R_2{}^2(9)$ and $R_2{}^2(8)$ motifs [79,80], respectively. The crystal packing of the molecules of **2** and **3a** along the ***b*** axis and along the ***c*** axes reveals *zigzag* layering of the molecules. In addition, the specific C–H$_{\text{methoxy}}$. . .N interaction in **3a** produces $C_1{}^1(8)$ chains along the *b* axis. The hydrogen atoms are given in light green for clarity. The detected π-π stacking interactions for the nitrobenzene/3,4,5-trimethoxy phenyl rings in **3a** (**c**) and for the phenyl/3,4,5-trimethoxy phenyl rings in **3d** (**d**) are illustrated.

3.3. Differential Scanning Calorimetry Studies

The thermal properties of compounds **2**, **3a–e** in dynamic nitrogen atmosphere was studied with differential scanning calorimetry (Figure 4 and Figures S49–S54). The DSC thermogram of the aldimine compound **2** (Figure S49) reveals a thermal stability up to around 110 °C when a sharp and intensive endothermic effect starts to develop. This endothermic effect, with a maximum temperature at 127.39 °C (H = 106.86 J/g), corresponds to the melting of compound **2**. As confirmed from XRD, NMR, and HR-MS analyses, the synthesized quaternary ammonium aldimine derivatives **3a–e** are pure, highly crystalline materials; therefore, it is expected that sharp endothermic effects of melting should be observed on their respective DSC thermograms. However, the DSC thermograms of **3a–e** reveal only sharp, intensive exothermic effects with maxima at 217.43 °C (H = 119.36 J/g), 251.80 °C (H = 165.28 J/g), 232.50 °C (H = 139.62 J/g), 221.35 °C (H = 136.72 J/g) and 206.77 °C (H = 119.05 J/g), respectively, probably corresponding to a rapid decomposition. The absence of a melting effect for **3a–e** could be explained by the lower activation energy required for the molecules to decompose than the energy required to break down the crystal lattice. Nevertheless, the studied compounds are thermally stable at least up to 110 °C (**2**) or up to 200 °C (**3a–e**) and do not have any solvents trapped in their crystal structure; therefore, they are suitable for biological experiments.

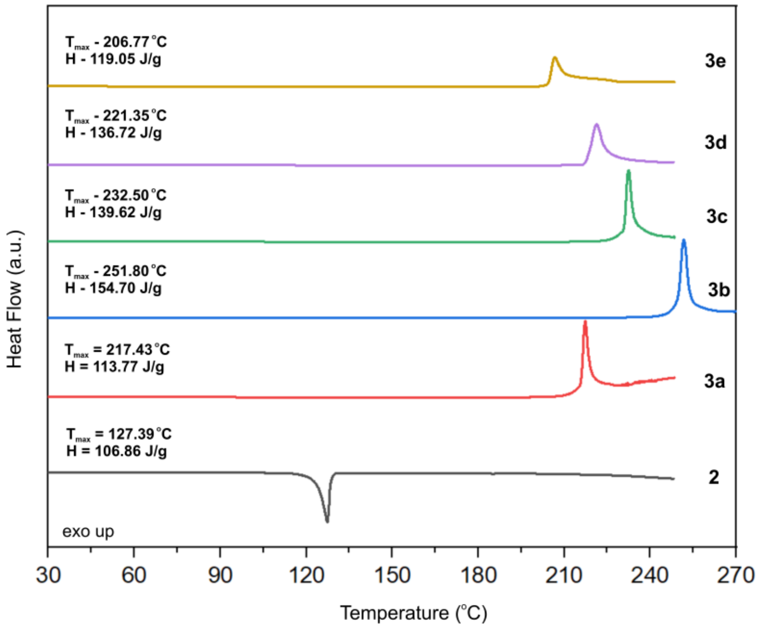

Figure 4. Graphical representation of the DSC thermograms of compounds **2**, **3a**–**e** with the appropriate color scheme. The maxima of the endothermic/exothermic effects corresponding to the melting/decomposition temperatures and the normalized enthalpy (H, J/g) are denoted.

3.4. Antioxidant Activity Studies

The radical scavenging activity and the ferric-reducing power of compounds **2**, **3a**–**e** were assessed with DPPH and FRAP assays, respectively, using Trolox as a referent (Figure 5). The evaluation of the antioxidant power of the investigated compounds was conducted by comparing the respective Trolox equivalent (TE) values (given in mM TE per gram ± *sd*) obtained from the corresponding calibration curves. A higher Trolox equivalent value suggests that the sample has a greater ability to neutralize free radicals or reactive oxygen species, which are associated with oxidative stress and various diseases. According to the DPPH assay, the radical scavenging activity values of the reported compounds is lower compared to Trolox and decrease in the following order: **2** (0.564 ± 0.017) > **3a** (0.240 ± 0.019) > **3c** (0.160 ± 0.022) ≅ **3e** (0.151 ± 0.027) ≅ **3b** (0.136 ± 0.022) ≅ **3d** (0.135 ± 0.039). The FRAP assay shows a similar trend with values for the ferric-reducing power decreasing in the following order: **2** (2.097 ± 0.025) > **3a** (1.250 ± 0.028) > **3e** (0.934 ± 0.005) > **3d** (0.873 ± 0.020) ≅ **3b** (0.864 ± 0.036) > **3c** (0.734 ± 0.014). According to both assays, compounds **2** and **3a** show better antioxidant activity compared to the other investigated compounds. Moreover, **2** and **3a** have slightly better ferric-reducing power compared to Trolox.

The DPPH assay is centered around the reduction of the DPPH stable free radical (DPPH•) to its non-radical form (DPPH-H) under the influence of an antioxidant (AO) molecule, while the FRAP assay involves the reduction of ferric ions (Fe^{3+}) to ferrous ions (Fe^{2+}) by reacting a Fe^{3+}-TPTZ complex with an AO at acidic conditions. In terms of mode of action, antioxidants can operate via hydrogen atom transfer (HAT) or single-electron transfer (SET) mechanisms. The reduction of DPPH• to DPPH-H can occur through simultaneous or sequential HAT and SET mechanisms (depending on the nature of the antioxidant and reaction conditions), while the reduction of Fe^{3+} to Fe^{2+} occurs predominantly through a SET mechanism. The overall radical scavenging activity not exceeding that of Trolox can be explained by the absence of strong proton donating groups in **2**, **3a**–**e** required to reduce the DPPH• radical to its non-radical state DPPH-H. The FRAP antioxidant activity suggests that **2**, **3a**–**e** possess reducing capabilities, which may involve the donation of electrons to reduce ferric ions to ferrous ions.

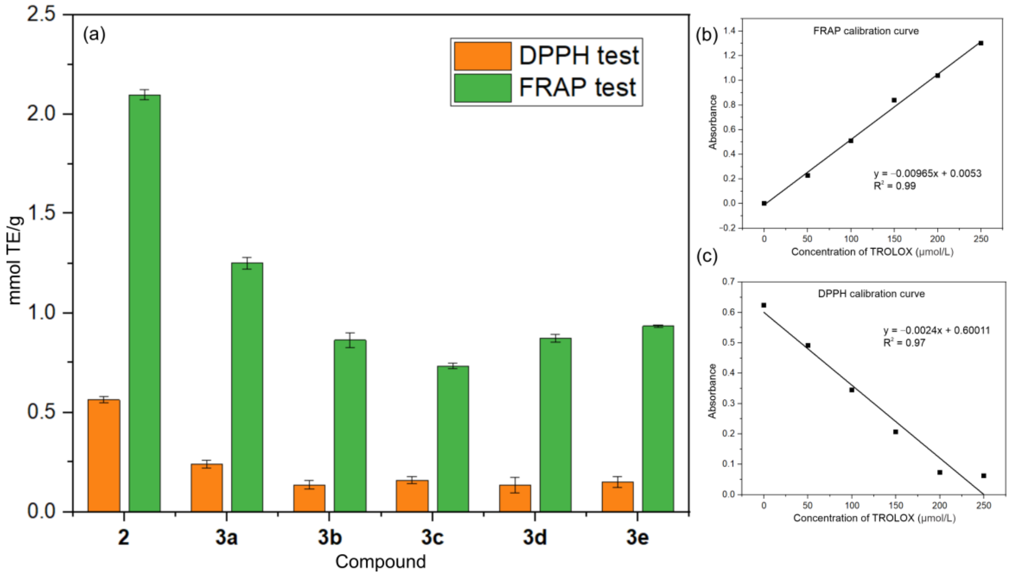

Figure 5. (**a**) Bar graph showing a comparison of DPPH radical scavenging activity (in orange) and ferric-reducing power of compounds **2**, **3a**–**e** expressed as Trolox equivalents (in green), (**b**) Frap calibration curve and (**c**) DPPH calibration curve.

3.5. Antibacterial Susceptibility Testing and Activity

Compounds **2**, **3a–e** were screened for antibacterial activity against *E. coli*, *S. aureus*, *K. pneumoniae*, and *P. aeruginosa* using Kirby–Bauer disk-diffusion method.

The Gram-negative *K. pneumoniae*, *P. aeruginosa*, and *E. coli* and the Gram-positive *S. aureus* were chosen as bacterial targets as they are representative of different groups, encompass a variety of resistance mechanisms, and are associated with diverse types of infections, including clinical infections. This variety allows for comprehensive testing of antibacterial agents, and the results for specific bacteria can be informative for broader applications against similar pathogens.

The inhibition zones produced by 30 μg of compounds **2**, **3a–e** were compared to those produced by the same amount of the reference antibiotic Kanamycin. The results from the antibacterial screening (Table 1) reveal that compounds **2**, **3a–e** have no antibacterial effect at the given concentration against *E. coli* and *S. aureus*, but demonstrate some selective antibacterial activity against *K. pneumoniae* and *P. aeruginosa*. More specifically, the most potent compounds from the series are nitrobenzene (**3a**) and benzodioxepine (**3b**) derivatives with inhibition zones of 15 mm and 12 mm against *K. pneumoniae.* The inhibition zone for compound **3e** is around 9 mm, almost half those of Kanamycin and **3a**.

Table 1. Measured inhibition zone (mm ± *sd*) of compounds **2**, **3a**–**e** against *E. coli*, *S. aureus*, *K. pneumoniae*, and *P. aeruginosa*.

	Inhibitory Diameter (mm ± *sd*), 30 μg/Disk			
	E. coli	***S. aureus***	***K. pneumoniae***	***P. aeruginosa***
2	–	–	7.8 (0.3)	–
3a	–	–	15.1 (0.3)	9.4 (0.4)
3b	–	–	11.9 (0.3)	7.1 (0.4)
3c	–	–	8.0 (0.2)	–
3d	–	–	7.5 (0.2)	7.2 (0.3)
3e	–	9.5 (0.3)	8.5 (0.4)	9.5 (0.3)
KAN	18.1 (0.4)	16.1 (0.4)	18.3 (0.6)	15.2 (0.3)

Compounds **3a**, **3b**, and **3e** were further investigated using the broth microdilution method to determine their minimum inhibitory concentration against *K. pneumoniae* (Figure 6). The obtained MIC values for **3a**, **3b**, and **3e** are around 500 μg/mL. The comparison with the MIC value of Kanamycin (14 μg/mL) suggests that these compounds exhibit significantly lower antibacterial activity against *K. pneumoniae* compared to Kanamycin. This indicates that while compounds **3a**, **3b**, and **3e** have some inhibitory effects, they are much less potent than Kanamycin. The broth microdilution method was also applied to determine the minimum inhibitory concentration of **3a**, **3b**, and **3e** against *P. aeruginosa*. Here, the results did not produce the expected effect (Figure S55), suggesting that these compounds are either ineffective against *P. aeruginosa* at the tested concentrations or that *P. aeruginosa* possesses mechanisms of resistance that render these compounds less effective. Further studies are required to elucidate the reasons behind the lack of efficacy and to explore potential modifications to improve their activity against these pathogens.

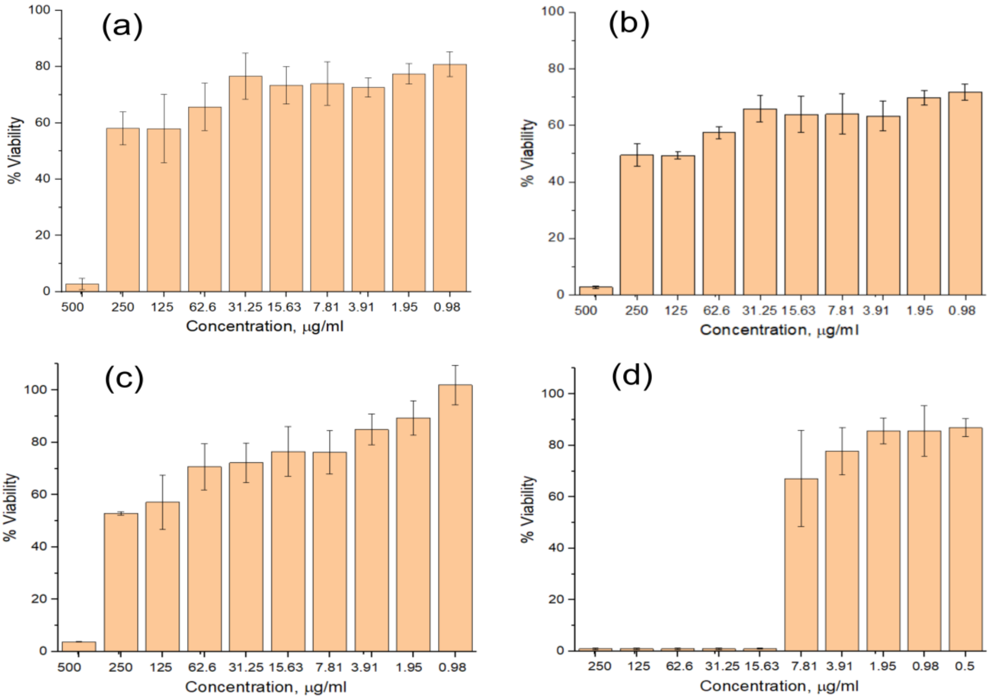

Figure 6. Dose-response curve of *K. pneumoniae* against compounds (**a**) **3a**, (**b**) **3b**, (**c**) **3e** and (**d**) kanamycin; the error bars represent the standard deviation of the experimental data.

Structurally, compounds **2**, **3a–e** are quite similar, all featuring common 3,4,5-trimethoxyphenyl and pyridine fragments connected via azomethine bond. The main differences between the reported compounds are in the –CH_2–C(=O)– bridged aromatic moieties and their specific functional groups. The almost linear molecular geometry of **2**, **3a–e** is conserved, despite the presence of flexible –CH=N– and (–CH_2–C(=O)–) bridging groups. Rotational freedom of the aromatic rings positioned on each side of the bridging groups is detected (Figure 2). The rotation of the TMP moiety is more pronounced as the detected twist angles between the mean planes of TMP and pyridine vary from 30.0° (**3c**) to 136.80° (in **2**). Compounds **2**, **3a–e** lack typical hydrogen bond donors, although hydrogen bond acceptors are available. From a molecular point of view, the synthesized **3a–e** can be compared with traditional/commercial QAS, i.e., they feature a positively charged nitrogen center. Thus, for **3a–e**, the antibacterial mechanism of action could be similar to QAS, involving electrostatic interactions between the positively charged nitrogen atom and the negatively charged components of microbial cell membranes (e.g., phospholipids and proteins) leading to the disruption of membrane integrity, leakage of cellular contents, and ultimately cell death [81,82]. In this regard, the electrostatic potential maps of compounds **2**, **3a**, **3c**, and **3d** were calculated based on their crystal structure data using Crystal Explorer ver. 17.5 software [83] at the B3LYP/631G(d,p) level of theory (Figure 7). Figure 7a,b visualize the electrostatic potential maps of compound **3a** (most active compound against *K. pneumoniae*) and the map of the commercial antibacterial QAS—dequalinium. It is visible that both compounds demonstrate a specific distribution of the positive (in blue) and negative (in red) charge in their molecules resulting in the formation of dipole. This is not true for the less active compounds **2**, **3c** and **3d** (Figure 7c) that are mostly positively charged with partly negative charged domains around the electron-accepting functional groups (C=O, –CH=N– and O–CH_3). To verify the proposed link between molecular charge distribution and antibacterial activity we calculated the electrostatic potential map (EPM) of the most active quaternary ammonium compounds from our previous work [84], 1-(2-(2,4-Dimethoxyphenyl)-2-Oxoethyl)-4-(Pyrrolidin-1-yl)Pyridin-1-Ium Bromide (CCDC 1992661) and 1-(2-([1,1′-Biphenyl]-4-yl)-2-Oxoethyl)-4-(Pyrrolidin-1-yl) Pyridin-1-Ium Bromide (CCDC 1992660). Similarly, the obtained EPMs reveal two distinct positively and negatively charged regions (Figure 7d,e).

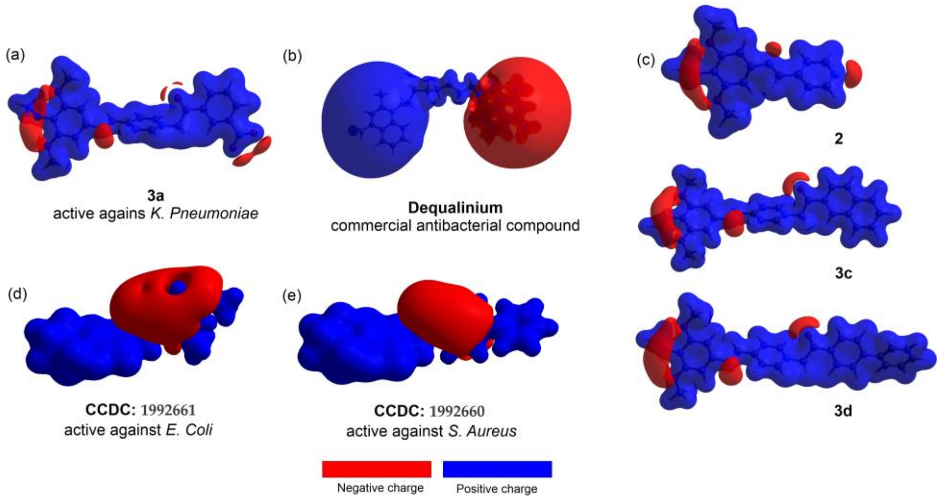

Figure 7. Electrostatic potentials maps calculate at the B3LYP/631G(d,p) level for compounds (**a**) **3a**, (**b**) dequalinium, (**c**) **2**, **3c** and **3d** (**d**) CCDC 1992661 and (**e**) CCDC 1992660.

In conclusion, the antibacterial activity of the studied quaternary ammonium aldimine derivatives is substituent driven but the effect requires the presence of opposite charges (positive and negative) at the extremities of the molecules. The selectivity of the antibacterial activity may be due to differences in membrane composition or susceptibility to membrane-disrupting agents among the tested bacterial species. Further research, involving the construction of a larger library of compounds and focusing on a specific bacterial strain, is needed to elucidate the specific molecular targets and mechanisms involved.

4. Conclusions

Herein, we have demonstrated the successful synthesis of five novel quaternary ammonium aldimine derivatives, each incorporating a 3,4,5-trimethoxy phenyl (TMP) fragment. The two-step synthetic methodology efficiency provided compounds in good yields and with high purity as confirmed by NMR and XRD analyses. The conducted single-crystal X-ray analysis disclosed a tendency towards conservation of the linear molecular geometry. A rotational freedom of the TMP and aromatics moieties around the bridging –CH=N– and (–CH_2–C(=O)–) fragment was disclosed. The crystal packing is dominated by weak C–H. . .O and $\pi \ldots \pi$ interactions. Compounds **2**, **3a**–**e** exhibited varying degrees of antioxidant activity, with some showing comparable FRAP activity to Trolox, although their radical scavenging activity was generally lower. The bacterial susceptibility testing using disk-diffusion method of these quaternary ammonium aldimine derivatives demonstrated selective antibacterial activity against Gram-negative bacteria *Klebsiella pneumoniae* and *Pseudomonas aeruginosa* for **3a**, **b**, **e**. The broth microdilution method was employed to determine **3a**, **b**, **e** MIC against *K. pneumoniae* and *P. aeruginosa.* Compounds **3a**, **3b**, and **3e** demonstrated some inhibitory effects against *K. pneumoniae*, although they are much less potent than Kanamycin. The BMD did not show inhibitory effects against *P. aeruginosa*. The selectivity of the antibacterial activity may be due to differences in membrane composition, interference through specific bacterial processes or pathways present in *K. pneumoniae* and *P. aeruginosa* but not in *E. coli*. The specific antibacterial activity was linked to a distinct charge separation visible on the electrostatic maps of the active compounds and the presence of specific substituents. The novel combination involving quaternary ammonium and aldimine derivatives reported herein not only add to the arsenal of potential antimicrobial and antioxidant agents but also offer a promising scaffold for further medicinal chemistry efforts aimed at combating microbial resistance.

Supplementary Materials: The following supporting information can be downloaded at: https://www.mdpi.com/article/10.3390/cryst14060486/s1; Figures S1–S6: ^{1}H NMR spectra of compounds **2**, **3a**–**e**, respectively; Figures S7–S12: ^{13}C NMR spectra of compounds **2**, **3a**–**e**, respectively; Figures S13–S17: ^{1}H-^{1}H NOESY spectra of compounds **3a**–**e**, respectively; Figures S18–S23: ^{1}H-^{13}C HSQC spectra of compounds **2**, **3a**–**e**, respectively; Figures S24–S29: ^{1}H-^{13}C HMBC spectra of compounds **2**, **3a**–**e**, respectively; Figures S30–S35: FT-IR spectra of compounds **2**, **3a**–**e**, respectively in the region of 4000–400 cm^{-1}; Figures S36–S41: HR-MS spectra in positive and negative mode of compounds **2**, **3a**–**e**, respectively; Figures S42–S46: Comparison between the powder XRD pattern of the bulk sample of compounds **2**, **3a**, **3c** and **3d**, respectively and the powder pattern generated from the single-crystal XRD experiment; Figures S44 and S47: Comparison between the powder XRD patterns of the bulk sample of compounds **3b** and **3e**, respectively and the powder patterns of the starting reagents for their synthesis; Figure S48: Representation of the detected halogen, hydrogen bonding interactions and short contacts (<sum of vdW radii) for compounds **2**, **3a**, **3c** and **3d**; Figures S49–S54: DSC thermograms of compounds **2**, **3a**–**e**, respectively; Figure S55: Dose-response curve of *P. aeruginosa* against compounds **3a**, **3b**, **3e** and Kanamycin; the error bars represent the standard deviation of the experimental data. Table S1: Most important crystallographic parameters obtained from the SCXRD of compounds **2**, **3a**, **3c** and **3d**; Tables S2–S5: Bond lengths for the crystal structure of compounds **2**, **3a**, **3c** and **3d**, respectively; Tables S6–S9: Bond angles for the crystal structure of compounds **2**, **3a**, **3c** and **3d**, respectively; Tables S10–S13: Torsion angles for the crystal structure of compounds **2**, **3a**, **3c** and **3d**, respectively; Table S14: Detected hydrogen bonding interactions and short contacts for the crystal structure of compound **2**; Tables S15–S17: Detected halogen bonding interactions and short contacts for the crystal structure of compounds **3a**, **3c** and **3d**, respectively.

Author Contributions: Conceptualization, R.R. and B.S.; formal analysis, R.R., V.K. and B.S.; visualization, R.R.; investigation, R.R., M.G. and B.S.; methodology, R.R., V.K., M.G. and B.S.; writing—original draft, R.R., B.S. and V.K.; funding acquisition, R.R. All authors have read and agreed to the published version of the manuscript.

Funding: This research was funded by the Bulgarian National Science Fund (BNSF), grant number KP-06-M59/7.

Data Availability Statement: The data of the current study are available from the corresponding authors upon reasonable request.

Acknowledgments: The authors acknowledge the technical support from project BG05M2OP001-1.002-0005, Perimed (2018–2023). The authors thank Zhanina Petkova for recording HRMS spectra.

Conflicts of Interest: The authors declare no conflict of interest.

References

1. Walsh, T.R.; Gales, A.C.; Laxminarayan, R.; Dodd, P.C. Antimicrobial Resistance: Addressing a Global Threat to Humanity. *PLoS Med.* **2023**, *20*, e1004264.
2. Tangcharoensathien, V.; Sunicha, C.; Angkana, S. Complex Determinants of Inappropriate Use of Antibiotics. *Bull. World Health Organ.* **2018**, *96*, 141–144. [CrossRef]
3. Brown, E.D.; Wright, G.D. Antibacterial Drug Discovery in the Resistance Era. *Nature* **2016**, *529*, 336–343. [CrossRef]

4. Luepke, K.H.; Suda, K.J.; Boucher, H.; Russo, R.L.; Bonney, M.W.; Hunt, T.D.; Mohr, J.F., III. Past, Present, and Future of Antibacterial Economics: Increasing Bacterial Resistance, Limited Antibiotic Pipeline, and Societal Implications. *Pharmacotherapy* **2017**, *37*, 71–84. [CrossRef]
5. Belete, T.M. Novel Targets to Develop New Antibacterial Agents and Novel Alternatives to Antibacterial Agents. *Hum. Microbiome J.* **2019**, *11*, 100052. [CrossRef]
6. Simoes, N.G.; Bettencourt, A.F.; Monge, N.; Ribeiro, I.A.C. Novel Antibacterial Agents: An Emergent Need to Win the Battle against Infections. *Mini Rev. Med. Chem.* **2017**, *17*, 1364–1376. [CrossRef]
7. Vila, J.; Moreno-Morales, J.; Ballesté-Delpierre, C. Current Landscape in the Discovery of Novel Antibacterial Agents. *Clin. Microbiol. Infect.* **2020**, *26*, 596–603. [CrossRef]
8. Wright, G.D. Opportunities for Natural Products in 21 St Century Antibiotic Discovery. *Nat. Prod. Rep.* **2017**, *34*, 694–701. [CrossRef]
9. Garcia-Gutierrez, E.; Mayer, M.J.; Cotter, P.D.; Narbad, A. Gut Microbiota as a Source of Novel Antimicrobials. *Gut Microbes* **2019**, *10*, 1–21. [CrossRef]
10. Romano, G.; Costantini, M.; Sansone, C.; Lauritano, C.; Ruocco, N.; Ianora, A. Marine Microorganisms as a Promising and Sustainable Source of Bioactive Molecules. *Mar. Environ. Res.* **2017**, *128*, 58–69. [CrossRef]
11. Walsh, C.T.; Wencewicz, T.A. Prospects for New Antibiotics: A Molecule-Centered Perspective. *J. Antibiot.* **2014**, *67*, 7–22. [CrossRef]
12. Wright, P.M.; Seiple, I.B.; Myers, A.G. The Evolving Role of Chemical Synthesis in Antibacterial Drug Discovery. *Angew. Chem. Int. Ed.* **2014**, *53*, 8840–8869. [CrossRef]
13. Mitcheltree, M.J.; Pisipati, A.; Syroegin, E.A.; Silvestre, K.J.; Klepacki, D.; Mason, J.D.; Terwilliger, D.W.; Testolin, G.; Pote, A.R.; Wu, K.J.Y.; et al. A Synthetic Antibiotic Class Overcoming Bacterial Multidrug Resistance. *Nature* **2021**, *599*, 507–512. [CrossRef]
14. Sinn, E.; Harris, C.M. Schiff Base Metal Complexes as Ligands. *Coord. Chem. Rev.* **1969**, *4*, 391–422. [CrossRef]
15. Yamada, S. Advancement in Stereochemical Aspects of Schiff Base Metal Complexes. *Coord. Chem. Rev.* **1999**, *190*, 537–555. [CrossRef]
16. Bilyj, J.K.; Silajew, N.V.; Bernhardt, P.V. Nickel Coordination Chemistry of Bis(Dithiocarbazate) Schiff Base Ligands; Metal and Ligand Centered Redox Reactions. *Dalton Trans.* **2021**, *50*, 612–623. [CrossRef]
17. Goel, A.; Malhotra, R. Efficient Detection of Picric Acid by Pyranone Based Schiff Base as a Chemosensor. *J. Mol. Struct.* **2022**, *1249*, 131619. [CrossRef]
18. Jafari, H.; Ameri, E.; Rezaeivala, M.; Berisha, A.; Halili, J. Anti-Corrosion Behavior of Two N_2O_4 Schiff-Base Ligands: Experimental and Theoretical Studies. *J. Phys. Chem. Solids* **2022**, *164*, 110645. [CrossRef]
19. Al Zoubi, W.; Ko, Y.G. Schiff Base Complexes and Their Versatile Applications as Catalysts in Oxidation of Organic Compounds: Part I. *Appl. Organomet. Chem.* **2017**, *31*, e3574. [CrossRef]
20. Paşa, S.; Arslan, N.; Meriç, N.; Kayan, C.; Bingül, M.; Durap, F.; Aydemir, M. Boron Containing Chiral Schiff Bases: Synthesis and Catalytic Activity in Asymmetric Transfer Hydrogenation (Ath) of Ketones. *J. Mol. Struct.* **2020**, *1200*, 127064. [CrossRef]
21. Gusev, A.N.; Kiskin, M.A.; Braga, E.V.; Kryukova, M.A.; Baryshnikov, G.V.; Karaush-Karmazin, N.N.; Minaeva, V.A.; Minaev, B.F.; Ivaniuk, K.; Stakhira, P. Schiff Base Zinc (II) Complexes as Promising Emitters for Blue Organic Light-Emitting Diodes. *ACS Appl. Electron. Mater.* **2021**, *3*, 3436–3444. [CrossRef]
22. Nayak, A.; Naik, P.H.B.; Teja, H.B.; Kirthan, B.R.; Viswanath, R. Synthesis and Opto-Electronic Properties of Green Light Emitting Metal Schiff Base Complexes. *Mol. Cryst. Liq. Cryst.* **2021**, *722*, 67–75. [CrossRef]
23. Imran, S.; Taha, M.; Ismail, N.H.; Khan, K.M.; Naz, F.; Hussain, M.; Tauseef, S. Synthesis of Novel Bisindolylmethane Schiff Bases and Their Antibacterial Activity. *Molecules* **2014**, *19*, 11722–11740. [CrossRef]
24. Nair, R.; Shah, A.; Baluja, S.; Chanda, S. Synthesis and Antibacterial Activity of Some Schiff Base Complexes. *J. Serb. Chem. Soc.* **2006**, *71*, 733–744. [CrossRef]
25. Yousif, E.; Majeed, A.; Al-Sammarrae, K.; Salih, N.; Salimon, J.; Abdullah, B. Metal Complexes of Schiff Base: Preparation, Characterization and Antibacterial Activity. *Arab. J. Chem.* **2017**, *10*, S1639–S1644. [CrossRef]
26. Miloud, M.M.; El-Ajaily, M.M.; Al-Noor, T.H.; Al-Barki, N.S. Antifungal Activity of Some Mixed Ligand Complexes Incorporating Schiff Bases. *J. Bacteriol. Mycol.* **2020**, *7*, 1122.
27. Joshi, R.; Kumari, A.; Singh, K.; Mishra, H.; Pokharia, S. Triorganotin (IV) Complexes of Schiff Base Derived from 1, 2, 4-Triazole Moiety: Synthesis, Spectroscopic Investigation, DFT Studies, Antifungal Activity and Molecular Docking Studies. *J. Mol. Struct.* **2020**, *1206*, 127639. [CrossRef]
28. Hazra, S.; Paul, A.; Sharma, G.; Koch, B.; Guedes da Silva, M.F.C.; Pombeiro, A.J.L. Sulfonated Schiff Base Sn(IV) Complexes as Potential Anticancer Agents. *J. Inorg. Biochem.* **2016**, *162*, 83–95. [CrossRef]
29. Gou, Y.; Li, J.; Fan, B.; Xu, B.; Zhou, M.; Yang, F. Structure and Biological Properties of Mixed-Ligand Cu(II) Schiff Base Complexes as Potential Anticancer Agents. *Eur. J. Med. Chem.* **2017**, *134*, 207–217. [CrossRef]
30. Ramadhan, U.H.; Haddad, H.M.; Ezaria, Z.G. Synthesis of Schiff Bases Complexes as Anti-Inflammatory Agents. *World J. Pharm. Pharm. Sci.* **2016**, *5*, 98–108.
31. Azam, M.; Al-Resayes, S.I.; Trzesowska-Kruszynska, A.; Kruszynski, R.; Shakeel, F.; Soliman, S.M.; Alam, M.; Khan, M.R.; Wabaidur, S.M. Zn(II) Complex Derived from Bidentate Schiff Base Ligand: Synthesis, Characterization, DFT Studies and Evaluation of Anti-Inflammatory Activity. *J. Mol. Struct.* **2020**, *1201*, 127177. [CrossRef]

32. Jarrahpour, A.; Shirvani, P.; Sharghi, H.; Aberi, M.; Sinou, V.; Latour, C.; Brunel, J.M. Synthesis of Novel Mono- and Bis-Schiff Bases of Morpholine Derivatives and the Investigation of Their Antimalarial and Antiproliferative Activities. *Med. Chem. Res.* **2015**, *24*, 4105–4112. [CrossRef]
33. Shaikh, I.; Travadi, M.; Jadeja, R.N.; Butcher, R.J.; Pandya, J.H. Crystal Feature and Spectral Characterization of Zn(II) Complexes Containing Schiff Base of Acylpyrazolone Ligand with Antimalarial Action. *J. Indian Chem. Soc.* **2022**, *99*, 100428. [CrossRef]
34. Wang, Y.-Y.; Xu, F.-Z.; Zhu, Y.-Y.; Song, B.; Luo, D.; Yu, G.; Chen, S.; Xue, W.; Wu, J. Pyrazolo[3,4-d]pyrimidine Derivatives Containing a Schiff Base Moiety as Potential Antiviral Agents. *Bioorg. Med. Chem. Lett.* **2018**, *28*, 2979–2984. [CrossRef]
35. Mansour, M.A.; AboulMagd, A.M.; Abdel-Rahman, H.M. Quinazoline-Schiff Base Conjugates: In Silico Study and ADMET Predictions as Multi-Target Inhibitors of Coronavirus (SARS-CoV-2) Proteins. *RSC Adv.* **2020**, *10*, 34033–34045. [CrossRef]
36. Anouar, E.H.; Raweh, S.; Bayach, I.; Taha, M.; Baharudin, M.S.; Di Meo, F.; Hasan, M.H.; Adam, A.; Ismail, N.H.; Weber, J.-F.F. Antioxidant Properties of Phenolic Schiff Bases: Structure–Activity Relationship and Mechanism of Action. *J. Comput. Aided Mol. Des.* **2013**, *27*, 951–964. [CrossRef]
37. Kumar, D.; Rawat, D.S. Synthesis and Antioxidant Activity of Thymol and Carvacrol Based Schiff Bases. *Bioorg. Med. Chem. Lett.* **2013**, *23*, 641–645.
38. Garcia, M.T.; Kaczerewska, O.; Ribosa, I.; Brycki, B.; Materna, P.; Drgas, M. Biodegradability and Aquatic Toxicity of Quaternary Ammonium-Based Gemini Surfactants: Effect of the Spacer on Their Ecological Properties. *Chemosphere* **2016**, *154*, 155–160. [CrossRef]
39. Kaneko, S.; Kumatabara, Y.; Shirakawa, S. A New Generation of Chiral Phase-Transfer Catalysts. *Org. Biomol. Chem.* **2016**, *14*, 5367–5376. [CrossRef]
40. Zhuravlev, O.E.; Kaftanov, A.D.; Yulmasov, G.S.; Voronchikhina, L.I. Synthesis and Thermal Stability of Bis-Quaternary Ammonium Ionic Liquids with Inorganic Anions. *Russ. J. Appl. Chem.* **2023**, *96*, 395–401. [CrossRef]
41. Yoganand, K.S.; Umapathy, M.J. Corrosion Inhibition Efficiency of Newly Synthesized Quaternary Ammonium Salt in 1M HCl. *Indian J. Chem. Technol.* **2022**, *29*, 68–74.
42. Kasibhatla, S.; Amarante-Mendes, G.P.; Finucane, D.; Brunner, T.; Bossy-Wetzel, E.; Green, D.R. Acridine Orange/Ethidium Bromide (AO/EB) Staining to Detect Apoptosis. *Cold Spring Harb. Protoc.* **2006**, *3*, pdb.prot4493. [CrossRef]
43. Kumar, R.; Saneja, A.; Panda, A.K. An Annexin V-FITC—Propidium Iodide-Based Method for Detecting Apoptosis in a Non-Small Cell Lung Cancer Cell Line. In *Lung Cancer: Methods in Molecular Biology*; Humana: New York, NY, USA, 2021; pp. 213–223.
44. Feoktistova, M.; Geserick, P.; Leverkus, M. Crystal Violet Assay for Determining Viability of Cultured Cells. *Cold Spring Harb. Protoc.* **2016**, *4*, pdb.prot087379. [CrossRef]
45. Basilico, N.; Migotto, M.; Ilboudo, D.P.; Taramelli, D.; Stradi, R.; Pini, E. Modified Quaternary Ammonium Salts as Potential Antimalarial Agents. *Bioorg. Med. Chem.* **2015**, *23*, 4681–4687. [CrossRef]
46. Zhang, L.; Feng, X.-Z.; Xiao, Z.-Q.; Fan, G.-R.; Chen, S.-X.; Liao, S.-L.; Luo, H.; Wang, Z.-D. Design, Synthesis, Antibacterial, Antifungal and Anticancer Evaluations of Novel β-Pinene Quaternary Ammonium Salts. *Int. J. Mol. Sci.* **2021**, *22*, 11299. [CrossRef]
47. Jin, G.; Xiao, F.; Li, Z.; Qi, X.; Zhao, L.; Sun, X. Design, Synthesis, and Dual Evaluation of Quinoline and Quinolinium Iodide Salt Derivatives as Potential Anticancer and Antibacterial Agents. *ChemMedChem* **2020**, *15*, 600–609. [CrossRef]
48. Zhang, W.; Chang, Y.; Zhong, W.; Zhang, A.; Lin, Y. Antifungal Mechanisms of Polymeric Quaternary Ammonium Salts against Conidia of *Fusarium oxysporum* f. sp. cubense, Race 4. *Eur. J. Plant Pathol.* **2023**, *165*, 317–331. [CrossRef]
49. Peng, Y.; Chang, J.; Xiao, Z.; Huang, J.; Xu, T.; Chen, S.; Fan, G.; Liao, S.; Wang, Z.; Luo, H. Synthesis and Antifungal Activity of Novel Tetrahydrogeranyl Quaternary Ammonium Salts. *Nat. Prod. Commun.* **2022**, *17*. [CrossRef]
50. Masters, P.A.; O'Bryan, T.A.; Zurlo, J.; Miller, D.Q.; Joshi, N. Trimethoprim-Sulfamethoxazole Revisited. *Arch. Intern. Med.* **2003**, *163*, 402–410. [CrossRef]
51. Allegra, C.J.; Chabner, B.A.; Tuazon, C.U.; Ogata-Arakaki, D.; Baird, B.; Drake, J.C.; Simmons, J.T.; Lack, E.E.; Shelhamer, J.H.; Balis, F. Trimetrexate for the Treatment of Pneumocystis Carinii Pneumonia in Patients with the Acquired Immunodeficiency Syndrome. *New Engl. J. Med.* **1987**, *317*, 978–985. [CrossRef]
52. Vogelzang, N.J.; Weissman, L.B.; Herndon, J.E., 2nd; Antman, K.H.; Cooper, M.R.; Corson, J.M.; Green, M.R. Trimetrexate in Malignant Mesothelioma: A Cancer and Leukemia Group B Phase II Study. *J. Clin. Oncol.* **1994**, *12*, 1436–1442. [CrossRef]
53. Sarris, A.H.; Phan, A.; Duvic, M.; Romaguera, J.; McLaughlin, P.; Mesina, O.; King, K.; Medeiros, L.J.; Rassidakis, G.Z.; Samuels, B. Trimetrexate in Relapsed T-Cell Lymphoma with Skin Involvement. *J. Clin. Oncol.* **2002**, *20*, 2876–2880. [CrossRef]
54. Canel, C.; Moraes, R.M.; Dayan, F.E.; Ferreira, D. Podophyllotoxin. *Phytochemistry* **2000**, *54*, 115–120. [CrossRef]
55. Zhang, W.; Gou, P.; Dupret, J.-M.; Chomienne, C.; Rodrigues-Lima, F. Etoposide, an Anticancer Drug Involved in Therapy-Related Secondary Leukemia: Enzymes at Play. *Transl. Oncol.* **2021**, *14*, 101169. [CrossRef]
56. Yan, J.; Sun, J.; Zeng, Z. Teniposide Ameliorates Bone Cancer Nociception in Rats Via the P2X7 Receptor. *Inflammopharmacology* **2018**, *26*, 395–402. [CrossRef]
57. Slobodnick, A.; Shah, B.; Pillinger, M.H.; Krasnokutsky, S. Colchicine: Old and New. *Am. J. Med.* **2015**, *128*, 461–470. [CrossRef]
58. Nam, N.-H. Combretastatin A-4 Analogues as Antimitotic Antitumor Agents. *Curr. Med. Chem.* **2003**, *10*, 1697–1722. [CrossRef]
59. Gerova, M.S.; Stateva, S.R.; Radonova, E.M.; Kalenderska, R.B.; Rusew, R.I.; Nikolova, R.P.; Chanev, C.D.; Shivachev, B.L.; Apostolova, M.D.; Petrov, O.I. Combretastatin A-4 Analogues with Benzoxazolone Scaffold: Synthesis, Structure and Biological Activity. *Eur. J. Med. Chem.* **2016**, *120*, 121–133. [CrossRef]

60. Atanasov, G.; Rusew, R.I.; Gelev, V.M.; Chanev, C.D.; Nikolova, R.; Shivachev, B.L.; Petrov, O.I.; Apostolova, M.D. New Heterocyclic Combretastatin A-4 Analogs: Synthesis and Biological Activity of Styryl-2(3H)-Benzothiazolones. *Pharmaceuticals* **2021**, *14*, 1331. [CrossRef]
61. Jian, X.-E.; Yang, F.; Jiang, C.-S.; You, W.-W.; Zhao, P.-L. Synthesis and Biological Evaluation of Novel Pyrazolo[3,4-b]Pyridines as Cis-Restricted Combretastatin A-4 Analogues. *Bioorg. Med. Chem. Lett.* **2020**, *30*, 127025. [CrossRef]
62. Morales, S.; Guijarro, F.G.; Ruano, J.L.G.; Cid, M.B. A General Aminocatalytic Method for the Synthesis of Aldimines. *J. Am. Chem. Soc.* **2014**, *136*, 1082–1089. [CrossRef]
63. Coates, J. Interpretation of Infrared Spectra, a Practical Approach. In *Encyclopedia of Analytical Chemistry*; Meyers, R.A., Ed.; Wiley: Chichester UK, 2000; Volume 12, pp. 10815–10837.
64. Degen, I.A. Detection of the Methoxyl Group by Infrared Spectroscopy. *Appl. Spectrosc.* **1968**, *22*, 164–166. [CrossRef]
65. Nandiyanto, A.B.D.; Oktiani, R.; Ragadhita, R. How to Read and Interpret FTIR Spectroscope of Organic Material. *Indones. J. Sci. Technol.* **2019**, *4*, 97–118. [CrossRef]
66. Bruker, AXS. *Inc. Apex 4. Bruker Advanced X-ray Solutions*; Bruker AXS Inc.: Madison, WI, USA, 2022.
67. Bruker, APEX. *Saint and Sadabs*; Bruker AXS Inc.: Madison, WI, USA, 2009.
68. Sheldrick, G.M. Shelxt–Integrated Space-Group and Crystal-Structure Determination. *Acta Crystallogr. Sect. A* **2015**, *71*, 3–8. [CrossRef] [PubMed]
69. Sheldrick, G.M. Crystal Structure Refinement with Shelxl. *Acta Crystallogr. Sect. C* **2015**, *71*, 3–8. [CrossRef]
70. Dolomanov, O.V.; Bourhis, L.J.; Gildea, R.J.; Howard, J.A.K.; Puschmann, H. Olex2: A Complete Structure Solution, Refinement and Analysis Program. *J. Appl. Crystallogr.* **2009**, *42*, 339–341. [CrossRef]
71. Farrugia, L.J. Wingx and Ortep for Windows: An Update. *J. Appl. Crystallogr.* **2012**, *45*, 849–854. [CrossRef]
72. Macrae, C.F.; Sovago, I.; Cottrell, S.J.; Galek, P.T.A.; McCabe, P.; Pidcock, E.; Platings, M.; Shields, G.P.; Stevens, J.S.; Towler, M. Mercury 4.0: From Visualization to Analysis, Design and Prediction. *J. Appl. Crystallogr.* **2020**, *53*, 226–235. [CrossRef]
73. Brand-Williams, W.; Cuvelier, M.E.; Berset, C. Use of a Free Radical Method to Evaluate Antioxidant Activity. *LWT-Food Sci. Technol.* **1995**, *28*, 25–30. [CrossRef]
74. Benzie, I.F.F.; Strain, J.J. The Ferric Reducing Ability of Plasma (FRAP) as a Measure of 'Antioxidant Power': The FRAP Assay. *Anal. Biochem.* **1996**, *239*, 70–76. [CrossRef]
75. Schneider, C.A.; Rasband, W.S.; Eliceiri, K.W. NIH Image to ImageJ: 25 years of image analysis. *Nat. Methods* **2012**, *9*, 671–675. [CrossRef]
76. Arnett, E.M.; Reich, R. Electronic effects on the Menshutkin reaction. A complete kinetic and thermodynamic dissection of alkyl transfer to 3-and 4-substituted pyridines. *J. Am. Chem. Soc.* **1980**, *102*, 5892–5902. [CrossRef]
77. Sola, M.; Lledos, A.; Duran, M.; Bertran, J.; Abboud, J.L.M. Analysis of solvent effects on the Menshutkin reaction. *J. Am. Chem. Soc.* **1991**, *113*, 2873–2879. [CrossRef]
78. Castejon, H.; Wiberg, K.B. Solvent effects on methyl transfer reactions. 1. The Menshutkin reaction. *J. Am. Chem. Soc.* **1999**, *121*, 2139–2146. [CrossRef]
79. Bernstein, J.; Davis, R.E.; Shimoni, L.; Chang, N.-L. Patterns in Hydrogen Bonding: Functionality and Graph Set Analysis in Crystals. *Angew. Chem. Int. Ed. Engl.* **1995**, *34*, 1555–1573. [CrossRef]
80. Grell, J.; Bernstein, J.; Tinhofer, G. Graph-Set Analysis of Hydrogen-Bond Patterns: Some Mathematical Concepts. *Acta Crystallogr. Sect. B Struct. Sci.* **1999**, *55*, 1030–1043. [CrossRef] [PubMed]
81. Denyer, S.P. Mechanisms of Action of Antibacterial Biocides. Int. Biodeterior. *Biodegradation* **1995**, *36*, 227–245. [CrossRef]
82. Ioannou, C.J.; Hanlon, G.W.; Denyer, S.P. Action of Disinfectant Quaternary Ammonium Compounds against Staphylococcus aureus. *Antimicrob. Agents Chemother.* **2007**, *51*, 296–306. [CrossRef] [PubMed]
83. Spackman, P.R.; Turner, M.J.; McKinnon, J.J.; Wolff, S.K.; Grimwood, D.J.; Jayatilaka, D.; Spackman, M.A. CrystalExplorer: A program for Hirshfeld surface analysis, visualization and quantitative analysis of molecular crystals. *J. Appl. Cryst.* **2021**, *54*, 1006–1011. [CrossRef] [PubMed]
84. Rusew, R.; Kurteva, V.; Shivachev, B. Novel Quaternary Ammonium Derivatives of 4-Pyrrolidino Pyridine: Synthesis, Structural, Thermal, and Antibacterial Studies. *Crystals* **2020**, *10*, 339. [CrossRef]